



# Experimental and Numerical Investigation of Stall Mechanism in Centrifugal Pump Impeller

X. D. Liu<sup>1</sup>, Y. J. Li<sup>1</sup>, Z. Q. Liu<sup>1,2†</sup> and W. Yang<sup>1</sup>

<sup>1</sup>College of Water Resources and Civil Engineering, China Agricultural University, Beijing 100083, China

<sup>2</sup>Beijing Engineering Research Center of Safety and Energy Saving Technology for Water Supply Network System, China Agricultural University, Beijing 100083, China

†Corresponding Author Email: [lzq@cau.edu.cn](mailto:lzq@cau.edu.cn)

(Received July 6, 2021; accepted December 25, 2021)

## ABSTRACT

Stall is a complex flow phenomenon in centrifugal pumps at part load conditions. However, there is no clear description of the stall evolution process and mechanism, which is critical for stall control. Based on a high-frequency Particle Image Velocimetry (PIV) system (10k Hz) and a non-refraction experimental bench, emphasis is laid on the flow structures near the initial stall conditions. The results show that as the flow rate decreased, the flow separation occurred at the middle of the blade suction side and then evolved into a stall vortex which moved to the impeller's inlet direction and kept growing. Subsequently, it broken into two vortices when reaching the location where the impeller cross-sectional area is the smallest. One stall vortex continued its motion toward the passage inlet direction, while the other vortex separates to the impeller outlet. As the stall vortex's size at the impeller inlet enlarged, the flow incident direction at the impeller inlet was directed to the blade suction side, which caused the stall vortex on the suction side to disappear. The stall mechanism is explained in detail using both experiments and numerical simulations. Meanwhile, the Scale Adaptive Simulation-Shear Stress Transport (SAS-SST) hybrid model is used to simulate several flow rate conditions near the stall initial stage. The findings indicate that the increasing adverse pressure gradient and the high-pressure zone move along the suction blade towards the impeller inlet as the flow rate is reduced; however, the relative velocity is constantly decreasing. When the fluid can't provide enough kinetic energy to maintain its continuous flow along the suction surface, flow separation occurs. The stall vortex, which results from flow separation, blocks the passage impeller. The increasing adverse pressure from the impeller outlet to the inlet is the main cause of flow separation; and the adverse pressure gradient is a major manifestation of the stall vortex.

**Keywords:** High-frequency PIV system; SAS-SST model; Stall evolution; Stall mechanism; Adverse pressure gradient.

## NOMENCLATURE

$n_s$	specific speed	$V$	mean absolute velocity
$n$	number of samples	$W$	tangential velocity
$P$	standard atmospheric pressure	$x$	Cartesian space coordinate
$Q_d$	design rate	$Y^+$	nondimensional wall distance
$R$	radius of the impeller	$Z$	number of blades
$r$	location of sampling line	$Re$	Reynolds number
$S$	impeller speed	$\rho$	density
$T$	blade thickness	$\Delta t$	time interval between two consecutive particle images
$U$	mean relative velocity	$\eta$	total pressure difference between two adjacent passages
$u$	velocity		

## 1. INTRODUCTION

The centrifugal pump is a type of widely used hydraulic machinery with complex features such as strong rotation, large curvature and multiple walls.

These structural features usually lead to rather complicated flow characteristics, like the stall at part load conditions. The occurrence of the stall vortex will affect flow uniformity negatively and generate intensely dynamic load (Guo and

Yoshiyuki 2005, Tanaka 2011, Zhao *et al.* 2018). In previous research, most scholars mainly focused on the stable stall vortex structure through experimental or numerical simulation methods. However, the flow characteristics of the initial stall conditions and the evolution process of the stall vortex play a key role on the study of the stall mechanism.

Emmons *et al.* (1955) used inline cascades as an example to investigate the stall propagation behavior for the first time. A clear explanation was described: with the decrease of the flow rate, flow separation occurs in the two impeller passages first due to some asymmetrical disturbance, resulting in stall vortex. Particle Image Velocimetry (PIV) is an important experimental method for studying the flow in a centrifugal pump. Most researchers (Sinha and Katz 2000, Wang and Tsukamoto 2003, Westra *et al.* 2010, Keller *et al.* 2014, Zhang *et al.* 2018, Wang *et al.* 2019) utilized the low-frequency PIV system to measure the flow field in the impeller. The sampling frequency of the early PIV system can only reach up to 15 Hz. Since the impeller speed is usually high, only phase-lock method can be used to obtain phase-averaged results. It means that the randomness and non-periodic characteristics of the stall phenomenon was modeled. Paone *et al.* (1989) were the first to observe the flow field structure in the impeller through the PIV system. They observed the stall phenomenon in a large area of the impeller under part-load conditions. Through the combination of PIV and Laser Doppler Velocimetry (LDV) technology, Pedersen (2000) discovered that the six-blade centrifugal pump emerged an alternating stall phenomenon in impeller passage at a part load condition. Although a stable stall vortex structure was observed, it is not clear how the stall vortex formed and evolved. Krause *et al.* (2005) studied the flow characteristics through the PIV system with a frequency of 50 Hz. The results indicated that when the rate condition  $Q/Q_d$  varies between 0.5 and 0.47, there was a stable fixed stall phenomenon in a certain passage. The rotating stall occurred in multiple flow passages when the flow rate was reduced to  $Q/Q_d = 0.41$ . Based on the phase-averaged flow field results in impeller, there are two main descriptions for the initial stall. One indicates that with the decrease of the impeller inlet flow rate, the generation of the stall vortex is due to the increase of the inflow angle from Luo *et al.* (2020). Another is that the stall vortex originated from the blade suction side or the pressure side obtained by Wang *et al.* (2019). Takeahi *et al.* (2002) analyzed the flow field inside the 7-blade impeller, and the measurement results showed that with the decrease of the impeller inlet flow rate, the stall in the impeller changed from a steady stall to a rotating stall. Westra *et al.* (2011) used PIV system to analyze the secondary flow inside the impeller. The existence of the secondary flow leads to the appearance of a low-velocity area near the suction side of the blade. Cui *et al.* (2013) found that the volute tongue has a significant effect on the flow field structure inside the impeller passage. When the impeller passage is close to the volute tongue, a

small vortex structure appeared on the suction side of the blade, and when the flow passage passes through the volute tongue, the vortex structure in the impeller flow passage was significantly weakened. Dazin *et al.* (2011) used air as the medium and measured the instantaneous flow field for a low specific speed centrifugal pump with seven blades. The sampling frequency of the PIV system is 980 Hz, and the results show the characteristics of the flow field in the bladeless area and the nonlinear mechanism between different flow phenomena. When the impeller is in part-load condition, the stall vortex in the impeller rotates around the impeller passages at a certain frequency. The evolution process of the stall vortex in passages is also an important basis for exploring the stall mechanism. Actually, the flow inside the centrifugal pump is rather complicated, and it is still difficult to accurately obtain the characteristics of the flow field inside the impeller. Therefore, a PIV system with a higher sampling frequency needs to be developed in order to thoroughly investigate the dynamic evolution of the stall vortex over time at the continuous impeller phase, which is of great significance to the study of the stall mechanism.

Numerical simulation is another effective method to study the stall mechanism of centrifugal pumps. Takeshi *et al.* (2004) used the  $k-\varepsilon$  turbulence model to predict the unstable flow characteristics, and mainly focused on the stall phenomenon in centrifugal pumps with guide vanes. The results show there is a close relationship between the number of guide vanes and the stall type. Zhang *et al.* (2014) also used the  $k-\varepsilon$  turbulence model to monitor the pressure pulsation in the volute of a six-blade centrifugal pump at the stall conditions. The simulation results show that in the early stage of the stall, the backflow on the blade suction side has little effect on the pressure pulsation in the volute. During a deep stall, the pressure pulsation produces an obvious excitation frequency. The Reynolds-averaged Navier-Stokes (RANS) models perform time-averaged processing for the flow field, which usually model the pulsating flow field characteristics, especially for pumps. Byskov *et al.* (2003) used the large eddy simulation (LES) method to calculate flow separation in a centrifugal pump for the first time. The simulation results show that the LES is closer to the experimental results, especially at part load conditions, in comparison with the RANS model. Huang *et al.* (2015) used an improved LES model to calculate the impeller flow field with a dual-passage method, which is only suitable for periodic symmetric flows. However, for non-periodic symmetric flows, this method has certain limitations. Zhou *et al.* (2017) compared the stall performance from five different subgrid-scale (SGS) turbulence models, and the results showed that different models obtained different results even under the same condition. Due to limitations in computing resources, the grid that was used by the aforementioned researchers does not strictly meet the requirements of the LES in theory. Byskov *et al.* (2003) used the second-order precision LES model to successfully predict the alternating stall phenomenon in experiment. However, different

from the PIV results, the stall vortex simulated by LES is located on the pressure surface of the blade, while the stall vortex measured by PIV is located on the suction side of the blade. With the development of turbulence models, the idea of the hybrid model using the RANS method in the near-wall area and the LES method in the far-away area has been widely used (Menter and Egorov 2010). Feng *et al.* (2010) used Detached Eddy Simulation (DES) to predict stall in the centrifugal pump. The results showed that DES could calculate the stall point. However, the simulation result had a large error in the prediction of the boundary layer, and there are gray areas in the RANS-LES area; this makes the model predict the transition prematurely. The scale adaptive simulation (SAS) method, which was proposed by Menter and Egorov (2005), has been successfully applied to flow analysis in rotating machinery (Younsi *et al.* 2008, Lucius 2010, Xia *et al.* 2014). In contrast to the LES method, the SAS model can obtain more accurate simulation results under relatively coarse grid conditions. Lucius (2010) studied the rotating stall phenomenon in a five-blade centrifugal pump based on the SAS-SST model; the results showed that the main frequency, which was calculated by the model, was consistent with the experimental results. Mathias *et al.* (2012) took the radial impeller outflow structure as the target and compared the prediction accuracy of the internal flow field in the centrifugal pump with different hybrid models including DES, SST and SAS. The results showed that the SAS model is more accurate compared to other hybrid models. Considering the simulation accuracy and computing resources, the SAS model is a better choice for predicting more flow field variables in centrifugal pumps.

The objective of this study is the experimental and numerical analysis of the flow characteristics of the initial stall conditions and the stall evolution process in a low specific speed impeller. First, the high-frequency PIV system with 10 k Hz and non-refraction rotating equipment were built to visualize the continuous flow field characteristics near the initial stall conditions and stall evolution process through the small flow rate gradient. Then, the SAS-SST model, which is verified by experimental results, was used to analyze the pressure field and adverse pressure gradient field. Finally, the stall mechanism is explained in depth using the combination of experiments and numerical simulations.

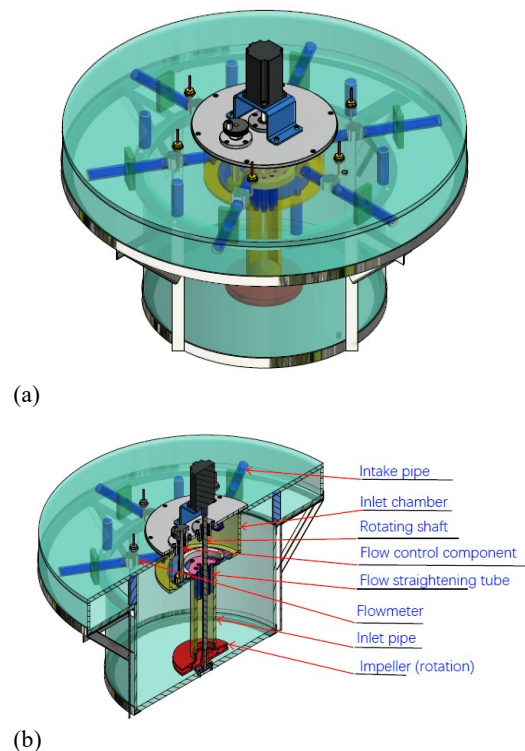
## 2. EXPERIMENTAL SETUP

### 2.1 Test device and impeller model

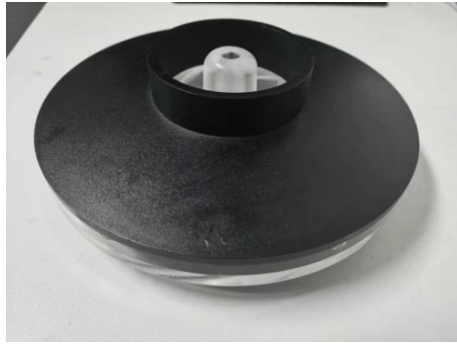
In the present work, a set of rotating machinery experimental bench, which was suitable for PIV observation without optical refraction, was independently developed. This experimental system mainly consisted of intake pipes, flow inlet chamber, flow control components, flow straightening tubes, turbine flow meter (0.5% measurement uncertainty), inlet pipe, and impeller and concentric adjustment components (as shown in

Fig. 1). The rotational speed (0.1% uncertainty) and the impeller were connected through the shaft. When the impeller rotated, the flow in the inlet pipe was sucked into the impeller. The water flowed out of the impeller and returned to the inlet chamber through the six circulation tubes. A flow meter was installed on each circulation tube to obtain accurate rates through the impeller. The flow control component was designed in the middle of the inlet chamber, to achieve tiny flow rate gradients. The complete experimental equipment was small in size but could realize the observation of internal flow characteristics for different impeller forms, speeds, and flow rates. At the same time, the laser incident conditions could be guaranteed and the laser energy loss could be reduced further.

An impeller of a low specific speed centrifugal pump ( $n_s = 3.65S\sqrt{Q}/H^{3/4} = 80$ ) without volute was designed for this investigation. The  $Q$  and  $H$  are the design flow rate and head of the impeller. The  $S$  is impeller rotating speed. The main design parameters are from the experimental centrifugal pump at the Technical University of Denmark (Pedersen 2000). An uneven image background and a mismatched refractive index are the two main factors that affect the image quality of particles. In contrast to the original impeller processing method, the impeller shroud is processed by a pure black acrylic plate, as shown in Fig. 2. In order to solve the problem of refractive index mismatch, a sodium iodide solution ( $I = 1.49$ ) was configured as the fluid medium. Figure 3 presents the comparison of a typical PIV particle image from sodium iodide solution and clean water, and indicates that the quality of particle images has been significantly improved after refractive index matching.



**Fig. 1. Experimental equipment: (a) whole structure, (b) internal structure.**



**Fig. 2. Impeller structure.**

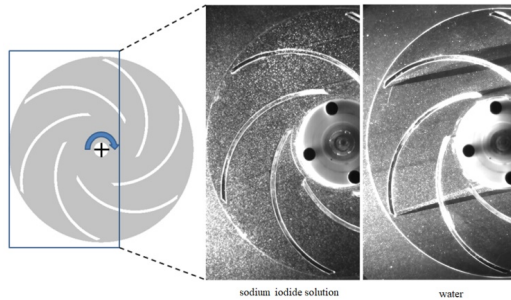


**Fig. 3. Overview of impeller and PIV measurement area (left) and a typical, PIV image (right).**

## 2.2 Experimental setup and conditions

In this study, a high-frequency PIV system, which mainly included a high-frequency laser, high-speed camera, synchronizer, and other auxiliary equipment were developed. The laser, with a repetition frequency of 10 kHz, was suitable for PIV. The high-speed camera could capture the particle images with a size of  $1920 \times 1080$  pixels, and the highest sampling rate is 20k Hz. The synchronizer was used to control both the laser and camera in order to complete the image collection. The tracer particles were made of hollow glass beads (density:  $1.1 \times 10^3 \text{ kg/m}^3$ , average diameter:  $10\mu\text{m}$ , refractive index: 1.5), which meet the basic requirements of non-toxic, clean, non-corrosive, non-wear, and stable chemical properties.

Figure 4 shows the non-refraction optical experimental bench and high-frequency PIV system. The entire experimental system was capable of continuously collecting particle images in the impeller at a frequency of 10 kHz. For example, if the impeller rotates at 725r/min, an instantaneous flow field result can be obtained when the impeller rotates 0.435 degrees. Based on the similarity law of the centrifugal pump, the experimental conditions were deduced at different impeller speeds. The flow rate gradient could reach approximately  $0.01Q_d$ , and the experimental system could capture the entire stall process from design conditions to part load conditions (as listed in Table 2). The time step between the two consecutive images of an image pair was 0.0001 s, and the duration of a complete measurement was 9s. A triple-pass cross-correlation method was used for determining the displacements from an image pair based on PIVLab (a program specially developed

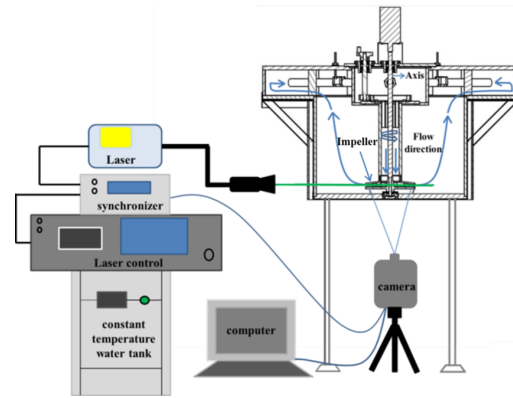


**Fig. 4. Experimental system.**

for PIV particle image analysis based on Matlab 16.0). The size of each interrogation area was  $32 \times 32$  pixels, with an overlap of 50%. Although high-frequency PIV system was used to measure the flow field inside the impeller, only the velocity components in the laser light plane are determined by two-dimensional PIV measurements. The axial component of the velocity is not measured. However, the results of Computational Fluid Dynamics (CFD) show that the out-of-plane velocity is sufficiently small for good PIV measurements. Meanwhile, sensitivity studies on the PIV processing have been performed to check the accuracy of the measured flow. The experimental uncertainties were evaluated according to [Abernethy \*et al.\* \(1985\)](#) for a 95% confidence level. Five separate measurements at rated conditions have been performed with an interval of one week. Excellent repeatability is obtained. The maximum uncertainties of the measured absolute velocity value  $UV=0.005$ . A comparison shows that the results are very similar, with differences in mean velocities below 0.2%. All the uncertainties are smaller than the symbol size in section 3.3, section 4.1 and 4.2.

## 3. NUMERICAL MODELING

### 3.1 The turbulence model

For the CFD computations, the commercial code ANSYS CFX 17.1 was employed. This code solves the time-dependent RANS equations that are discretized by a finite volume method, with an artificial compressibility method on a three-dimensional structured grid ([Maitre \*et al.\* 2013](#)). The semi-implicit method for pressure linked equations (SIMPLE) algorithm is used to solve the pressure-velocity coupling equation, with the hybrid scheme blending central differencing with second-order upwind spatial discretization for the convective flux terms and the second-order central discretization for the diffusion terms; the Hybrid Gauss-Least Squares method is used for gradient computation. The coordinate system applied in the impeller is a rotating reference while other parts use a stationary reference. Hence, the “frozen rotor-stator” and “transient rotor-stator” were imposed on the interface between the impeller and the outlet

section to simulate the real relative movement in steady state and transient simulations, respectively. The choice of turbulence model is the key to predict the accurate flow field. The SAS-SST is a scale-adaptive simulation model that uses an improved Unsteady Reynolds-averaged Navier-Stocks (URANS) method. Since the length scale of the SAS-SST model in the transport equation is based on the local von Karman length scale, the structure can be adjusted according to the flow field velocity in the unsteady simulation.

The SAS-SST model adds the source term  $Q_{SAS}$ , which contains the von Karman length scale, to the turbulent dissipation frequency equation in the transport equation. The model equations are given as follows:

$$\frac{\partial(\rho k)}{\partial t} + \frac{\partial(\rho u_i k)}{\partial x_j} = \frac{\partial}{\partial x_j} \left[ \left( \mu + \frac{\mu_t}{\sigma_k} \right) \frac{\partial k}{\partial x_j} \right] + P_k - c_{\mu} \rho k \omega \quad (1)$$

$$\begin{aligned} \frac{\partial(\rho \omega)}{\partial t} + \frac{\partial(\rho u_i \omega)}{\partial x_j} &= \frac{\partial}{\partial x_j} \left[ \left( \mu + \frac{\mu_t}{\sigma_{\omega}} \right) \frac{\partial \omega}{\partial x_j} \right] + \\ (1 - F_1) 2\rho \frac{1}{\sigma_{\omega 2} \omega} \frac{\partial k}{\partial x_j} \frac{\partial \omega}{\partial x_j} &+ \frac{\omega}{k} P_k - \beta \rho \omega^2 + Q_{SAS} \end{aligned} \quad (2)$$

In the above formula, the additional source term is expressed by Eq. (3):

$$\begin{aligned} Q_{SAS} &= \max \left[ \rho \zeta_2 \kappa S^2 \left( \frac{L}{L_{VK}} \right)^2 - C \cdot \frac{2\rho k}{\sigma_{\phi}} \right. \\ &\left. \max \left( \frac{1}{\omega^2} \frac{\partial \omega}{\partial x_j} \frac{\partial \omega}{\partial x_j}, \frac{1}{k^2} \frac{\partial \omega}{\partial x_j} \frac{\partial \omega}{\partial x_j} \right), 0 \right] \end{aligned} \quad (3)$$

In Eq. (3),  $\zeta_2 = 3.51$ ,  $\sigma_{\phi} = 2/3$ ,  $C = 2$ ,  $\kappa = 0.41$ ,  $c_{\mu} = 0.09$ ,  $L$  is the modeled turbulence length scale ( $L = \sqrt{k} / (c_{\mu}^{1/4} \cdot \omega)$ ). The expression of von Karman's length scale can be expressed as:

$$L_{VK} = \frac{\kappa S^2}{|U^n|} \quad U^n = \sqrt{\frac{\partial^2 U_i}{\partial x_k^2} \frac{\partial^2 U_i}{\partial x_j^2}} \quad (4)$$

$$S = \sqrt{2S_{ij}S_{ij}}, \quad S_{ij} = \frac{1}{2} \left( \frac{\partial U_i}{\partial x_j} + \frac{\partial U_j}{\partial x_i} \right) \quad (5)$$

To control the optimal damping of the turbulent kinetic energy, the  $L_{VK}$  can be expressed as:

$$L_{VK} = \max \left( \frac{\kappa S^2}{|U^n|}, C_s \sqrt{\frac{k \zeta_2}{(\beta / c_{\mu}) - \alpha}} \cdot \Delta \right), \quad \Delta = \Omega_{CV}^{1/3} \quad (6)$$

where  $\Omega_{CV}$  is the controlled volume. In the RANS area,  $Q_{SAS} = 0$ . In the SAS area:

$$\begin{aligned} Q_{SAS} &= \rho \zeta_2 \kappa S^2 \left( \frac{L}{L_{VK}} \right)^2 - C \cdot \frac{2\rho k}{\sigma_{\phi}} \\ &\max \left( \frac{1}{\omega^2} \frac{\partial \omega}{\partial x_j} \frac{\partial \omega}{\partial x_j}, \frac{1}{k^2} \frac{\partial \omega}{\partial x_j} \frac{\partial \omega}{\partial x_j} \right) \end{aligned} \quad (7)$$

This shows that the SAS-SST turbulence model uses the RANS method in the near-wall area and the approximate LES method in the far-away area. The additional source term  $Q_{SAS}$ , which is introduced by the turbulence model, is composed of the von Karman length scale. Its denominator is the second derivative of velocity, and the numerator is the expression of the velocity gradient, making the conversion of the SAS-SST model between RANS and LES dependent on local flow field characteristics.

According to the simplification of the experimental device, the calculation domain of the fluid consists of three parts: the inlet section, the impeller section and the outlet section. After comparing the influence of different inlet sizes on the interior of the impeller, the inlet extension was chosen to be 0.25D2 and the outlet extension was 0.06D2 (The size of the inlet and outlet section has been verified for irrelevance). The grid structure of the three sections is shown in Fig. 5.

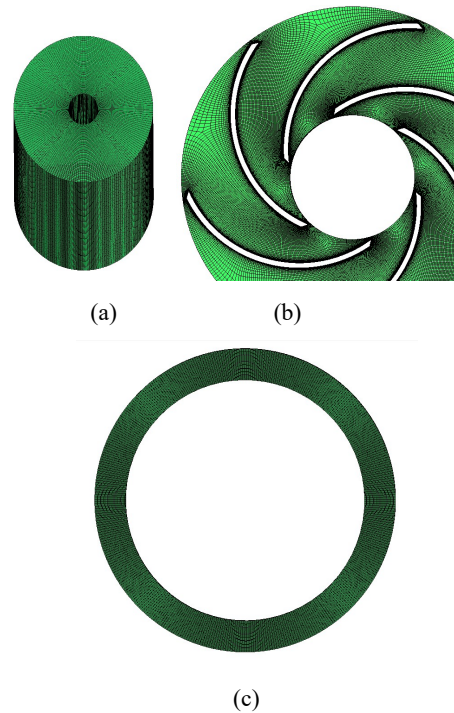


**Fig. 5. Computational domain: (a) inlet section, (b) impeller section, (c) outlet section.**

For the simulation domain, three types of boundaries are given: the velocity inlet was given on the inlet boundary based on the results from experiment and the turbulence quantities at inlet were set to 2% turbulence intensity and a turbulent length scale of 1/10 of the inlet diameter, the pressure outlet was given on the outlet boundary, and the mean static pressure was 0 Pa based on the environmental pressure of 1 atm. No-slip walls were set on the solid walls, including the blade, hub, and shroud. Here, the turbulent viscosity  $\nu_t$  is also set to zero. The initial condition of the flow field was

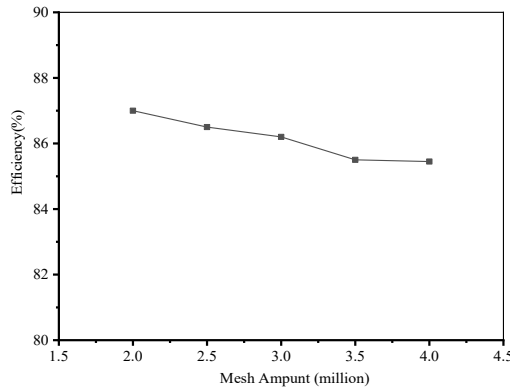


**Fig. 6. Comparison of efficiency under different grid numbers.**

from the steady result (calculated by the SST *k-w* model), and the SAS-SST model was used to predict the unsteady characteristics of the impeller under different rate conditions. The time step, analyzed was  $2.3 \times 10^{-4}$  s (equivalent to a pitch of  $2^\circ$ ), and the convergence criterion was  $1 \times 10^{-6}$  [28]. A total of 10 impeller cycles were calculated, and the results from the last five cycles were statistically averaged over time.

### 3.2 Grid independence verification

The mesh number was checked to balance the simulation accuracy and the time-cost. Structure mesh cells generated by ANSYS ICEM are utilized in inlet section and outlet section. Impeller section mesh cells are produced by ANSYS Turbogrid 17.1. Five sets of different numbers of grids with 2.0, 2.5, 3.0, 3.5 and 4 million were used to calculate the flow field. The impeller efficiency was used as the evaluation index for grid convergence as shown in Fig. 6. In order to further reduce the influence of the grid on flow characteristics, the relative velocity was used as the evaluation index. Since the flow field structure of the six passages of the impeller is basically the same, the mean relative velocity *U* of a single passage, at relative sampling line position  $r/R=0.5$  from impeller pressure side ( $\theta=0^\circ$ ) to suction side ( $\theta=60^\circ$ ) was selected for comparative analysis. The *W* is the circumferential velocity at the impeller exit. The *r* is the radius of sampling line location, and *R* is the radius of the impeller. The comparison results are shown in Fig. 7. Finally, the number of grids is chosen 3.5million.

The treatment of the near-wall area has an important influence on the simulation result. The near-wall area, which was based on the *k-w* model, adopted an automatic approximate wall processing model to obtain the velocity distribution near the wall. The automatic adjustment of the model was realized by the value of  $\omega$  in different regions; it was more sensitive to the grid in the solution of the viscous bottom layer. Therefore, for high-precision numerical simulations, the recommended grid  $Y^+$  was approximately 1. Figure 8 shows the  $Y^+$  distribution on the blade surface, which meets the calculation requirements of the model.

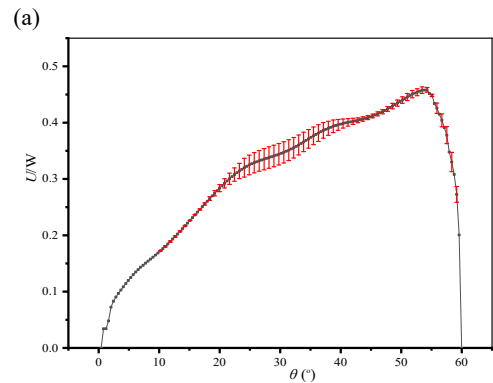
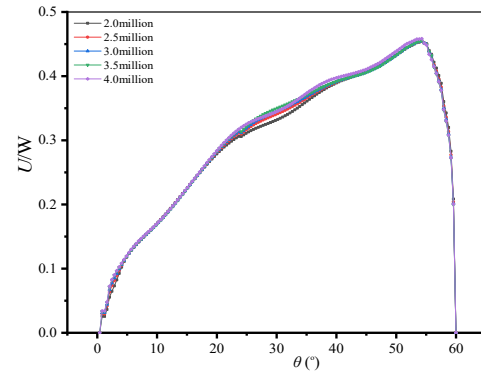


**Fig. 7. Comparison of relative velocity for different grid numbers: (a) relative velocity distribution, (b) discretization error bars.**

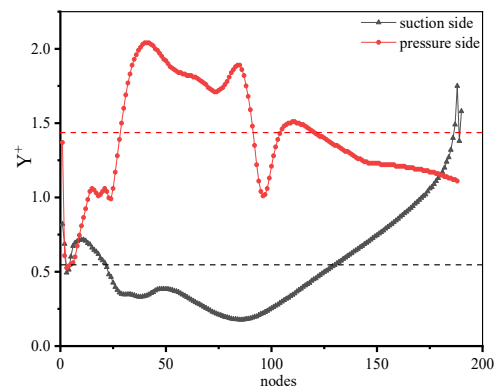


**Fig. 8.  $Y^+$  distribution on the blade surface.**

### 3.3 Verification of computational and experimental results

A numerical simulation method was used for predicting the flow field in the centrifugal pump impellers for different rate conditions. To confirm the accuracy of the results, verification was conducted. Figure 9 shows phase-averaged flow field of experiments and numerical simulations under part load conditions ( $S = 725$  r/min,  $Q = 0.3Q_d$ ). It shows that the results obtained by the numerical simulation and the experimental results are in good agreement independently of the number or shape of the vortices. Therefore, the prediction accuracy of the model was effectively verified. Next, the SAS-SST model was used to predict the

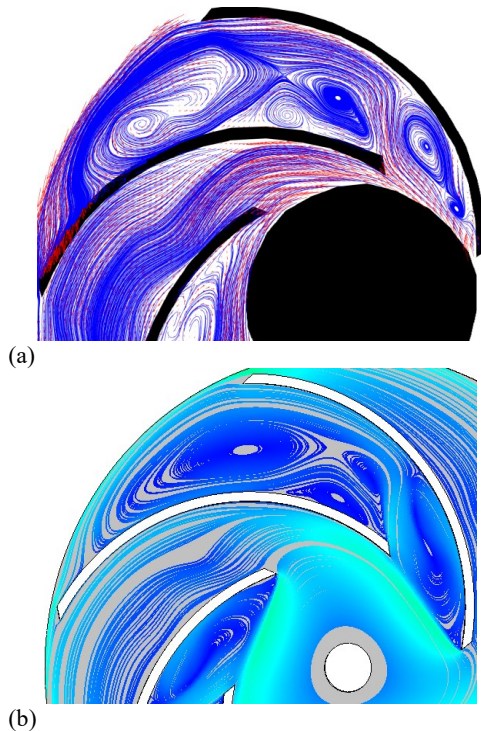


**Fig. 9. Comparison between experimental and numerical results: (a)  $S=725\text{r/min}$ ,  $Q=0.3Q_d$  (experiment), (b)  $S=725\text{r/min}$ ,  $Q=0.3Q_d$  (simulation).**

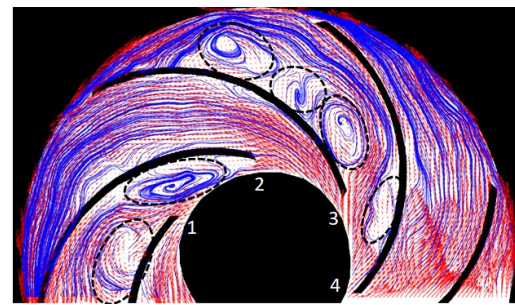
flow characteristics for the initial stall conditions to further explore its mechanism.

#### 4. RESULTS

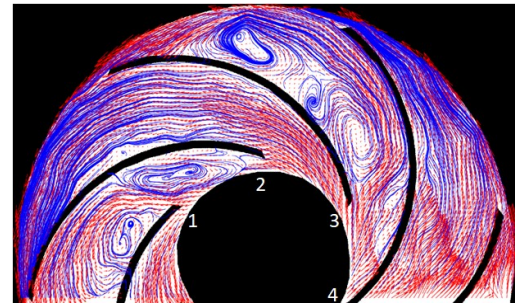
In this section, both the instantaneous and phase-averaged flow fields, which are represented by the magnitude of the relative velocity, are presented. Through the combination of velocity vector and streamline, the whole stall process from initial to final stability is shown. Then, the numerical simulation method is used to explore the stall mechanism.

##### 4.1 Instantaneous flow field results at different continuous phases in the impeller based on experiment.

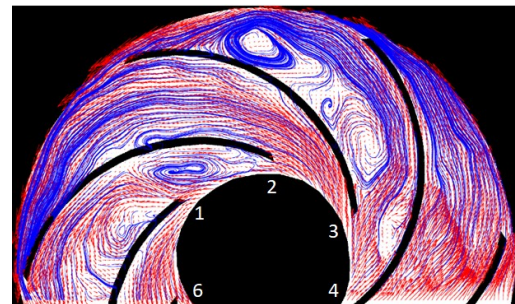
This experimental system could obtain the continuous flow field structure in the impeller and the flow field structure (depicted by vectors and streamlines) on the half-height plane of the blade is concerned. For the impeller speed of  $S = 600 \text{ r/min}$ , the instantaneous flow field could be obtained when the impeller rotated 0.36 degrees. The flow rate  $Q = 0.5Q_d$  was used as an example to show the flow field characteristics at different continuous phases. Since the angular interval between the two particle images was rather small, the instantaneous flow field is shown by the interval of 30 instantaneous results for better visualization of the impeller phase change. The impeller phase angle of the first frame of the instantaneous flow field was set at  $\varphi = 0^\circ$ , as shown in Fig. 10(a), and blades were numbered from 1 to 6. Through the observation of the velocity



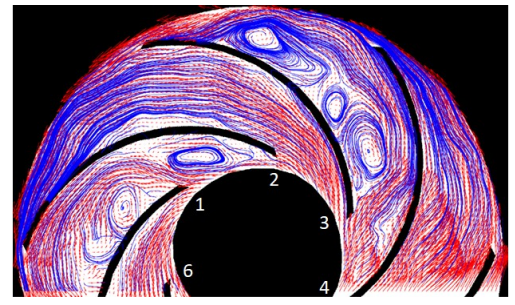
(a)  $\varphi = 0^\circ$



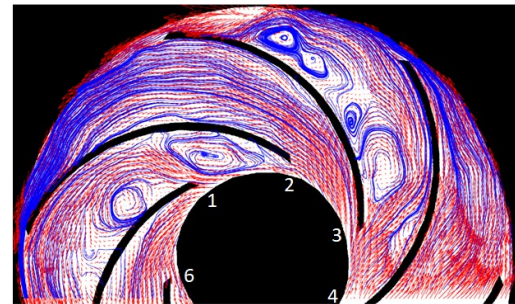
(b)  $\varphi = 10^\circ$



(c)  $\varphi = 20^\circ$



(d)  $\varphi = 30^\circ$



(e)  $\varphi = 40^\circ$

**Fig. 10. Instantaneous flow field structure inside the impeller at different phases.**

field under different continuous phases in the impeller, and for a certain flow rate, the shape of the stall vortex inside the impeller did not change significantly over time. Figure 10(a) shows that the black dotted ellipse masks the main vortexes and they are stationary relative to the blades at different impeller phase. To obtain clearer vortex structure distribution characteristics, the continuous velocity field in the impeller was processed using the phase-averaged method.

#### 4.2 Phase-averaged flow field based on image rotation method under different rate conditions

The entire process of the stall vortex from the initial generation ( $Q/Q_d = 0.72$ ), development, evolution, and finally, stability ( $Q/Q_d = 0.30$ ) were observed through tiny flow rate gradient. The main focus is mainly on the moment of the flow field at the beginning of the stall as presented in Fig. 11 (a) – (i). The impeller with six blades flowed out evenly in the circumferential direction. Two adjacent passage impellers were selected for analysis considering the uniform outflow in the circumferential direction of the impeller. The averaged relative velocity field under each rate condition was obtained from 100 instantaneous flow fields. Firstly, for the condition with non-stall flow, the flow in both passages A and B were close to the blade surface in Fig. 11 (a). With the flow

rate decreasing, the flow near the suction side of two impeller passages started to deviate and flow separation occurred in Fig. 11 (b); these are masked with green arrows. The flow separation on the suction side in passage A evolved into a rather small broken vortex structure (masked by the green oval) as the rate continued to decrease, and passage B continued to maintain the flow separation state without the appearance of vortex structure (shown in Fig. 11(c)). Then, the small broken vortex in passage A gradually evolved into stall vortex; passage B completely exited the critical stall, and the flow separation phenomenon near the suction side of the blade disappeared (shown in Fig. 11(d)). The size of the vortex structure continued to increase and moved towards the inlet of passage A, until it reached the location where the inlet cross-sectional area is smallest (shown in Fig. 11(e) – (f)). The complete stall vortex in passage A evolved into two individual stall vortexes as the rate continued to decrease (shown in Fig. 11(g)); this phenomenon is consistent with the vortex structure in the impeller observed by Krause *et al.* (2005). One of the stall vortexes continued to move towards the inlet of the impeller, and the other stall vortex moved back to the exit of the impeller. The size of the stall vortex in the inlet direction continued to increase, while the stall vortex in the outlet direction began to decrease. As the size of the stall vortex at the inlet increased, the incident direction (red arrow) of the inlet flow pointed to the suction side of the blade

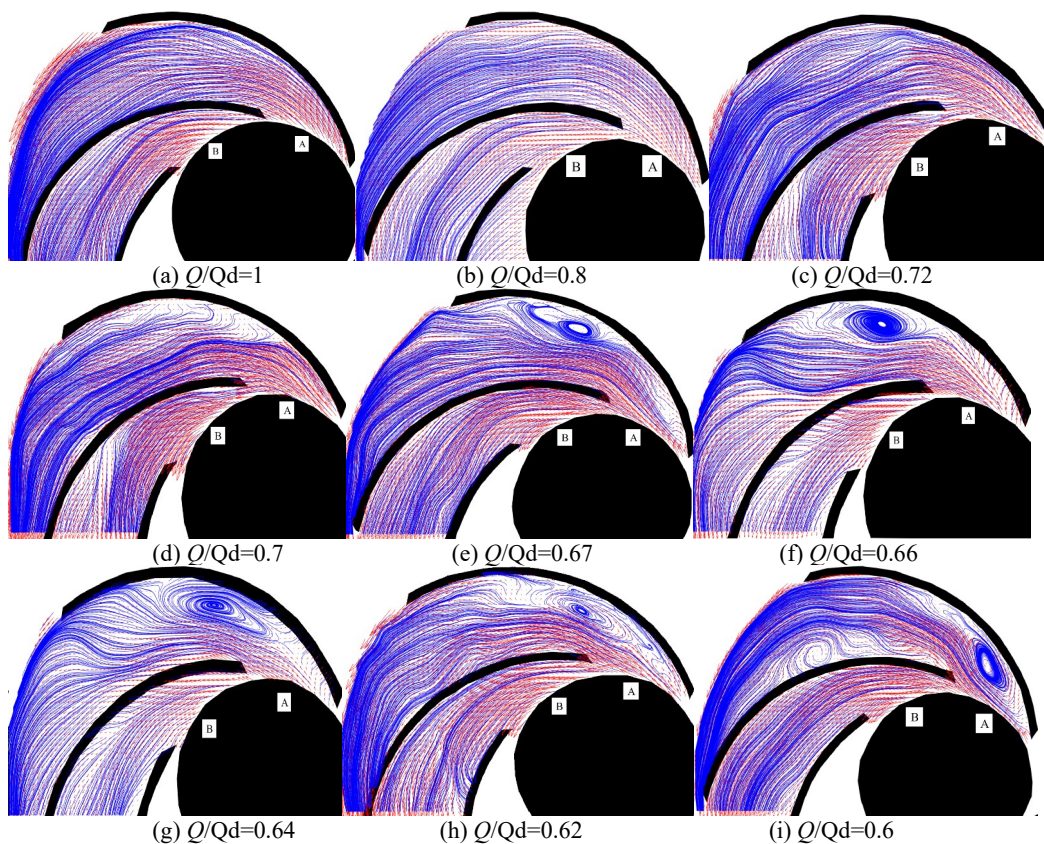


Fig. 11. Evolution of the stall in the impeller.

(shown in Fig. 11(g)). This resulted in the disappearance of the stall vortex on the suction side of the impeller. Since the main flow direction pointed to the suction side of the blade, the velocity on the pressure side of the impeller began to decrease and a big stall vortex began to appear (as shown in Fig. 11(h)). With further decrease of the rate, the stall vortex on the pressure surface continuously moved towards the inlet of the impeller and the big stall vortex evolved into two.

### 4.3 Numerical simulation results

Based on the PIV system, the fine velocity field inside the impeller could be obtained; the initial stall flow field and the stall evolution process could be clearly displayed through the instantaneous and mean flow fields. However, it was difficult to conduct a more in-depth study on the stall mechanism using only the velocity field results. After the verification from the experimental results, a numerical simulation method was used to analyze the characteristics of the pressure field, reverse pressure gradient field, and so on, under several rate conditions near the initial stall conditions, so as to further explore the stall mechanism.

#### 4.3.1 Analysis of velocity cloud under initial stall conditions and velocity value distribution on sampling lines at different radial positions

In the experiment, the actual rate gradient reached  $0.01Q_d$  or less by fine-tuning the valve opening. However, such a small rate gradient could also be achieved theoretically in the numerical simulation, but a lot of computing resources and time were

required. Therefore, the numerical simulation was conducted for several rate conditions. Velocity and pressure are the two most important and direct variables that characterize the characteristics of the flow field in the impeller. Although this paper mentions that the stall occurs because the kinetic energy is difficult to resist the reverse pressure energy as the flow rate decrease near suction side. However, based on the relationship between kinetic energy per unit mass and relative velocity:  $E=1/2V^2$ . Actually, the distribution trend of velocity and kinetic energy is consistent. In order to ensure the unity of variables, this paper mainly uses velocity and pressure to characterize the dynamic evolution process of stall. Figure 12 shows the results of the time-averaged flow field near the initial stall conditions.

The flow characteristics near the initial stall conditions were also analyzed through the velocity distribution. For the rated flow conditions in Fig. 12(a), the high velocity area mainly appeared on the suction side of the impeller inlet, while the low velocity area appeared on the suction side of the blade. This is consistent with the velocity distribution characteristics of general centrifugal pumps. For the rate condition  $Q/Q_d = 0.72$  in Fig. 12(b), the velocity distribution near the suction side blade changed significantly. The flow near the suction side began to separate. The appearance of flow separation resulted in a significant low-velocity area near the suction side blade. However, from the distribution of streamlines, it seemed there was no backflow vortex in passages. Besides, there was also a very small low-velocity area  $\alpha$  that was

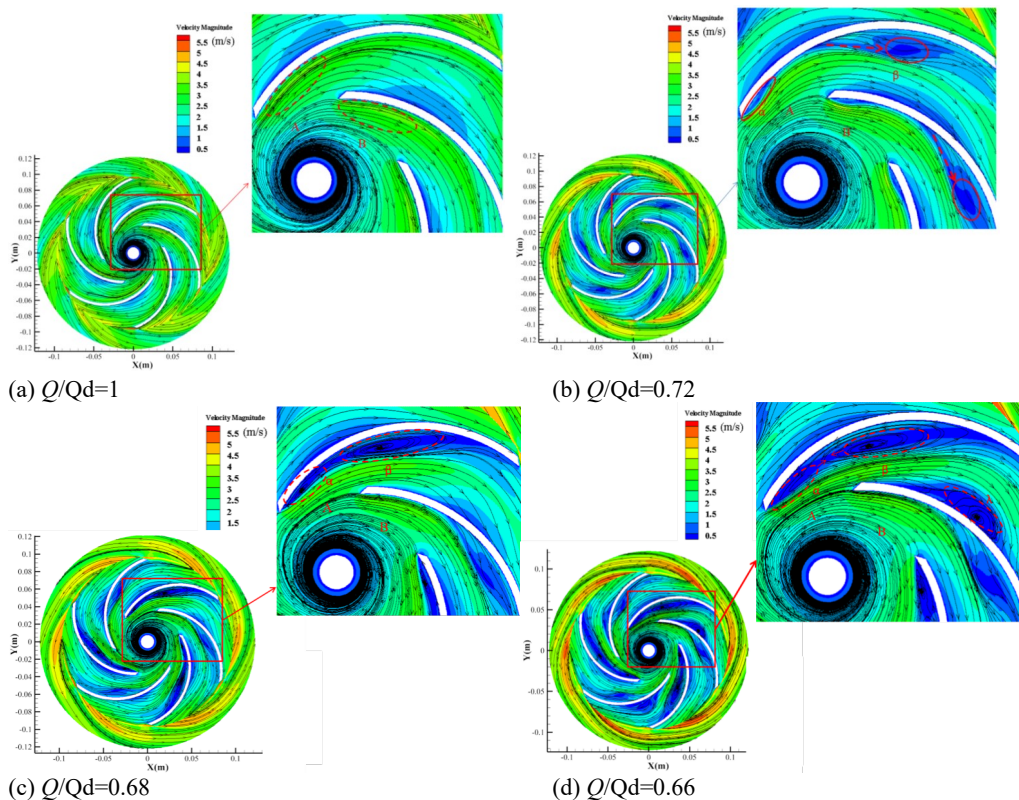


Fig. 12. Results of the time-averaged flow field in the impeller under initial stall conditions.

caused by increasing the incidence angle at the suction side inlet. The flow field structures in passage A and passage B were the same. However, with the further decrease of the rate in Fig. 12(c), the low-velocity area, which was caused by flow separation in passage A, reduced. An obvious low-velocity area  $\beta$  appeared at the position close to the suction side blade; meanwhile, the low-velocity area  $\alpha$ .

The mean relative velocity value at different relative radial positions during the stall process was compared in passage A and B and is shown in Fig. 13. It shows that under the design flow rate condition in Fig.13(a), the velocity from the pressure surface to the suction surface conforms to the trend of first increasing, and then, decreasing at the relative position ( $r/R = 0.44 - 0.75$ ). At the relative position ( $r/R = 0.82 - 0.95$ ), the velocity distribution was evenly distributed. This flow phenomenon is consistent with the flow field characteristics of the impeller under design flow rate conditions. With the rate decrease shown in Fig.13(b), the velocity distribution trend was the same as that under the rated working condition at the relative position ( $r/R = 0.44 - 0.56$ ). There is only a rather small vortex structure on the suction side of the blade inlet. When the flow bypasses the velocity zone, the flow returns to the suction side surface of the blade. As the flow area of the impeller passage expands, the flow velocity decreases, which leads to the obvious large-area low-velocity zone near the suction side of the blade. This indicates that the decrease in rate did not affect significantly the flow characteristics at the impeller inlet. For the relative sampling line positions ( $r/R > 0.62$ ), the velocity decreased rapidly at the position of  $\theta = 45^\circ$ . The range of the low-velocity area ( $r/R = 0.62 - 0.95$ ) in passage A was larger than that ( $r/R = 0.62 - 0.75$ ) in passage B. For the rate condition  $Q/Q_d=0.68$  (presented in Fig.13(c)), the relative position ( $r/R = 0.44 - 0.75$ ) in the low-velocity area appeared at  $\theta = 45^\circ$ ; when  $r/R > 0.82$ , the low-velocity area disappeared. When an obvious stall vortex structure appears near the suction side of the blade, a large area of low velocity appears in this area. The lowest value of the velocity in the impeller emerged at  $r/R = 0.56 - 0.62$ . For passage B, the range of the low-velocity area also further expanded ( $r/R=0.62-0.95$ ). The flow field characteristics in passage B under  $Q/Q_d=0.68$  conditions were very similar to those in passage A.

#### 4.3.2 Pressure distribution under initial stall conditions

From the results of the velocity distribution, it shows that the stall vortex in the impeller originated from the flow separation near the blade suction side. Based on the boundary layer flow separation theory, its essence is that the kinetic energy of the fluid can't fight against the reverse pressure. Therefore, how the pressure distribution difference in the impeller passages induced the stall was further analyzed. Figure 14 shows the total pressure distribution near initial stall conditions. Under rated flow conditions (Fig. 14(a)), it shows that the total pressure from the suction side to the pressure side is

symmetrical, but the total pressure at the suction side inlet is smaller than that on the pressure side inlet. As the rate decreases in Fig. 14(b); however, the total pressure distribution in the impeller passage is no longer symmetrical. The low-pressure area moves to the blade pressure side, and the high-pressure area extends along the suction side blade to the impeller inlet direction for both passages. As the high pressure continuously moves along the suction side of the blade to the inlet direction of the impeller, the speed near the suction side of the middle position of the blade starts to decrease as shown in Fig.12(b). For the rate conditions  $Q/Q_d = 0.68$  (Fig. 14(c)), it indicates that the high pressure area moves further to the impeller inlet direction in passage A. However, for flow passage B, the high pressure on the suction side of the blade inlet no longer continues to move to the inlet direction of the impeller; and the low-pressure area at the inlet position tends to move to the impeller outlet direction. When the pressure near the suction side in the passage B gradually decreases, it shows from Fig.12(c) that the velocity value at the corresponding position begins to gradually increase, so that the passage B exits the stall state. When the flow rate is further reduced (Fig. 14(d)), the high-pressure area further spreads along the suction side blade to the impeller inlet direction; the maximum pressure of the entire passage is located on the suction side blade in passage A.

Figure 15 shows the comparison of the pressure in passages A and B at different radial sampling line positions. The  $\eta = (P1-P2)/P$ , where P1 and P2 represent the total pressure at the corresponding positions of passage A and B, respectively, and  $P = 1$  Atm. Next, we further quantitatively analyzed how the difference in pressure distribution between two adjacent impeller passages affects the occurrence of stalls. In order to further highlight the difference between the two flow passages near the suction side of the blade, the angle range is selected from  $\theta=30^\circ-60^\circ$ . It shows that under rated conditions (Fig. 15(a)), the pressure distribution from the pressure side to the suction side of the two passages at different radii is similar; however, there are certain fluctuations at the impeller outlet position. It presents the distribution trend of the flow streamlines in the impeller passages are smooth. As the flow rate decreases (Fig. 15(b)), it shows that when the relative position  $r/R = 0.44 - 0.75$ , the pressure distribution in the two passages is the same. But, at the position close to the impeller outlet ( $r/R = 0.82 - 0.95$ ), it appears that the pressure on the suction side of passage A is greater than that in passage B. This indicates that for passage A, the high pressure firstly emerges along the suction side blade to the impeller inlet direction. At this time, the passage A and B have a similar flow separation tendency. However, for the position close to the outlet of the impeller, the pressure of the passage A is significantly greater than that of the passage B. This results in a lower velocity area near the suction side of the passage A. This phenomenon is also verified on the velocity magnitude distribution on the sampling line under this flow rate condition. As the flow rate decreases

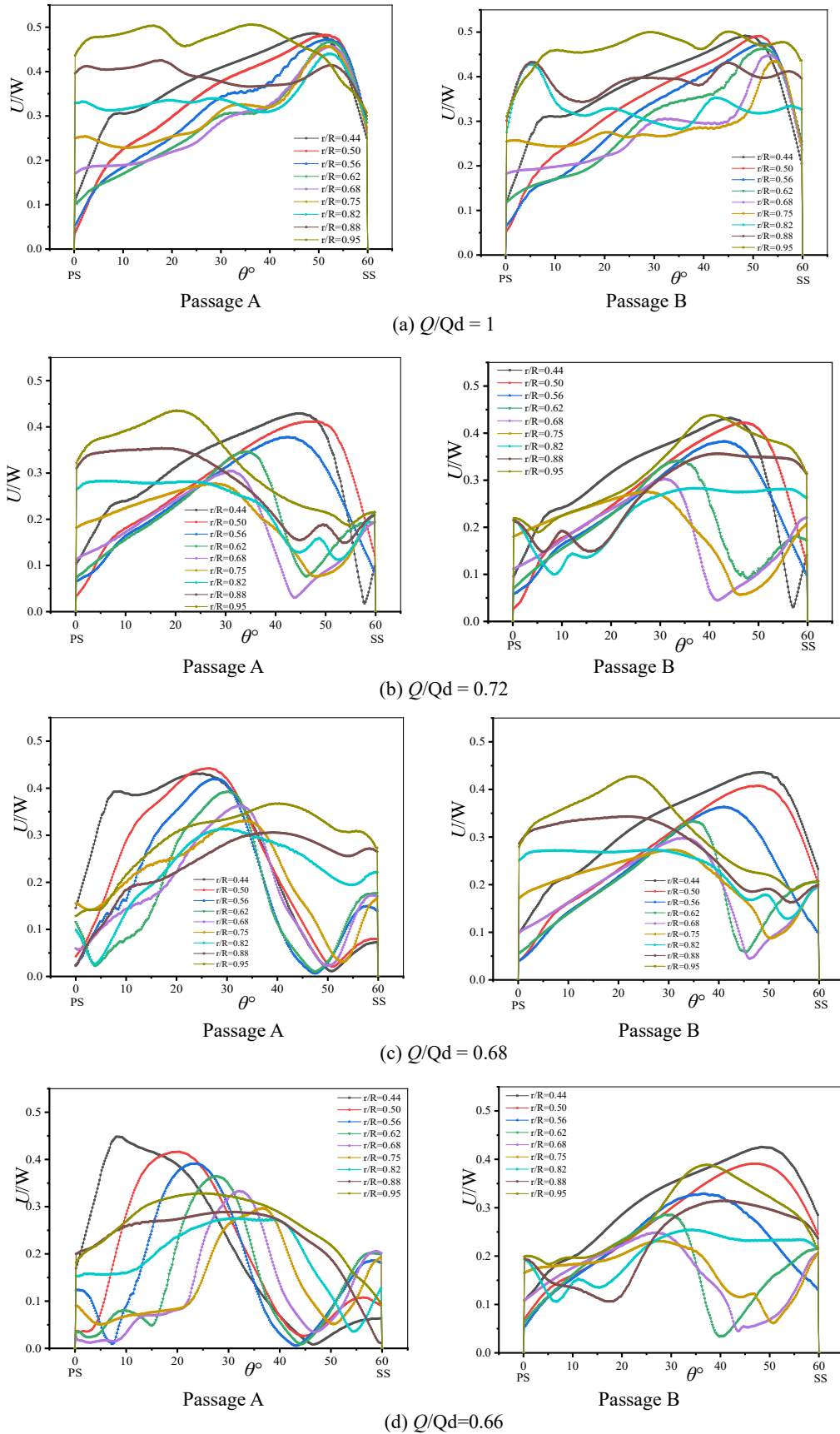


**Fig. 13.** Velocity value at different relative sampling line positions during the stall process in passages A and B.

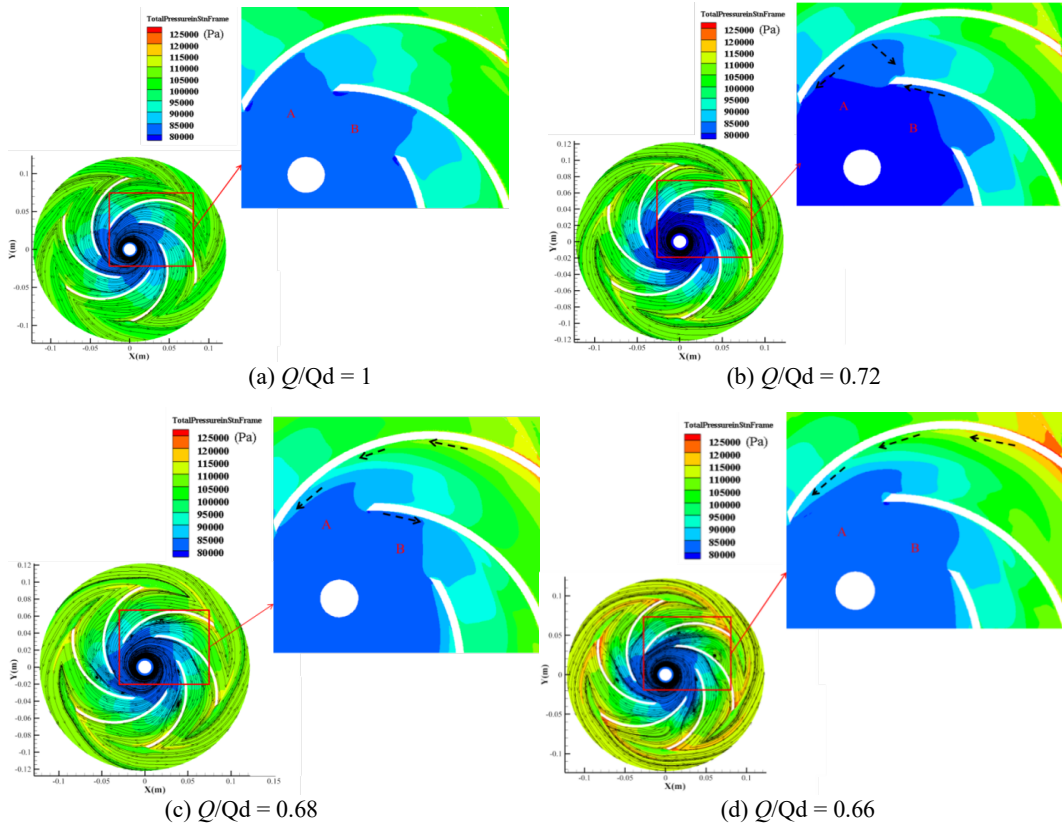


**Fig. 14.** Pressure distribution inside the impeller at initial stall conditions.

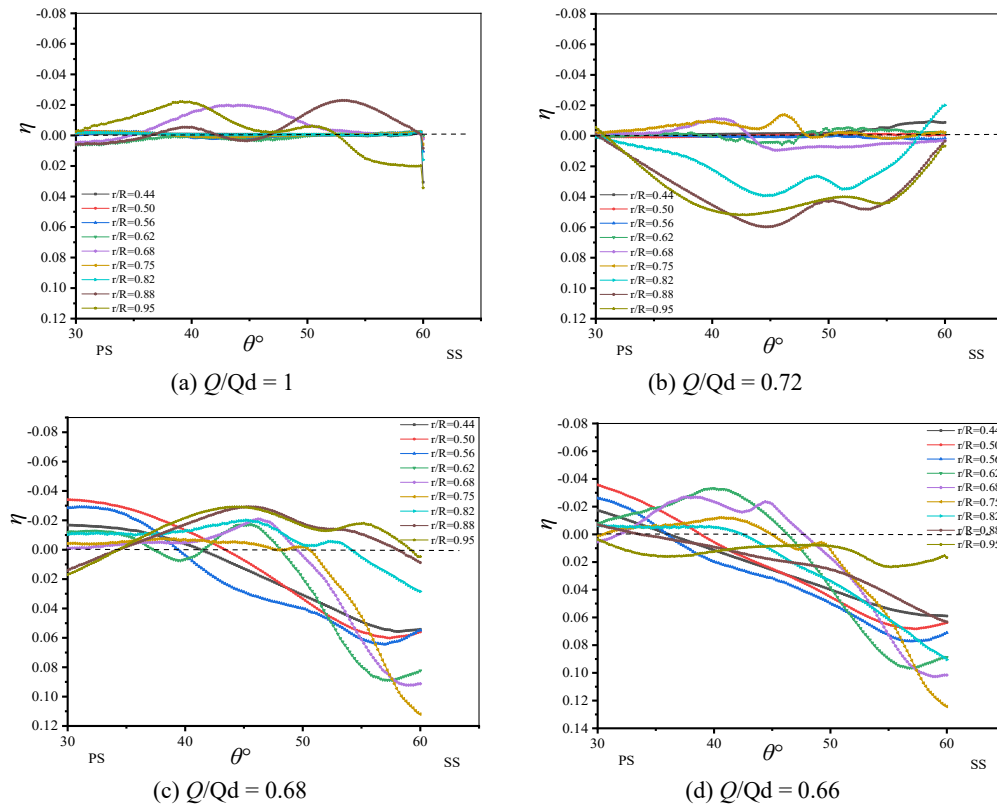


**Fig. 15.** Pressure comparison near the suction side blade in passages A and B under initial stall conditions.

further, the difference between the suction side of the two flow passages A and B becomes more obvious. As the pressure along the suction side in the passage A increases continuously, the velocity at this position is further reduced, and an obvious vortex structure begins to appear. For the rate condition  $Q/Q_d = 0.68$  (Fig. 15(c)), the pressure difference between the two flow passages is largest at the position where  $r/R = 0.62 - 0.75$ . At the position of the impeller outlet ( $r/R = 0.88 - 0.94$ ), the difference in pressure distribution between the two flow passages is the smallest. This indicates that as the flow decreases, the position where the pressure difference between the two flow passages is the largest continues to move towards the impeller inlet direction. Meanwhile, in contrast to the condition  $Q/Q_d = 0.72$ , the pressure distribution difference between the two passages is significantly increased. As the rate further decreases under the condition  $Q/Q_d = 0.66$  (Fig. 15(d)), The results show that at the position where  $r/R = 0.82 - 0.95$ , the pressure distribution difference between the two flow passages further increases, and basically, remains stable at the position where  $r/R = 0.44 - 0.75$ .

#### 4.3.3 Distribution of adverse pressure gradient in stall initial conditions

The above results indicate that the appearance of stall in the impeller was essential for the evolution of flow separation. Therefore, the reverse pressure gradient field was further analyzed under the initial

stall conditions. The reverse pressure gradient is a main feature of the flow field in a centrifugal pump. The vortex structure exists usually corresponds to higher reverse pressure gradient. For the special structure of the centrifugal pump, there is usually a stagnation point at the leading edge of the blade, which also leads a high reverse pressure gradient area. Under design conditions (Fig. 16(a)), there was a high value area of the adverse pressure gradient at the position of the impeller inlet and outlet, which was related to the strong shear. At the middle position of the passage impeller, the distribution of the reverse pressure gradient was relatively uniform, in the form of strips with high and low values. As the flow rate decreased (Fig. 16(b)), the high value area of the reverse pressure gradient appeared near the suction side blade. Based on the streamline, flow separation also occurred in the high value area of the reverse pressure gradient.

For the rate condition  $Q/Q_d = 0.68$  (Fig. 16(c)), the high value of the reverse pressure gradient appeared in the middle position of the suction side blade and extended in the form of a strip along the suction side blade to the impeller inlet direction. The high value area of the reverse pressure gradient was in good agreement with the position of the stall vortex. When the flow rate further reduced (Fig. 16(d)), the high-value reverse pressure gradient area further expanded, which corresponded to the larger-scale vortex. The essence of the reverse pressure gradient is a way of expressing pressure change, and an indirect manifestation of the vortex structure.

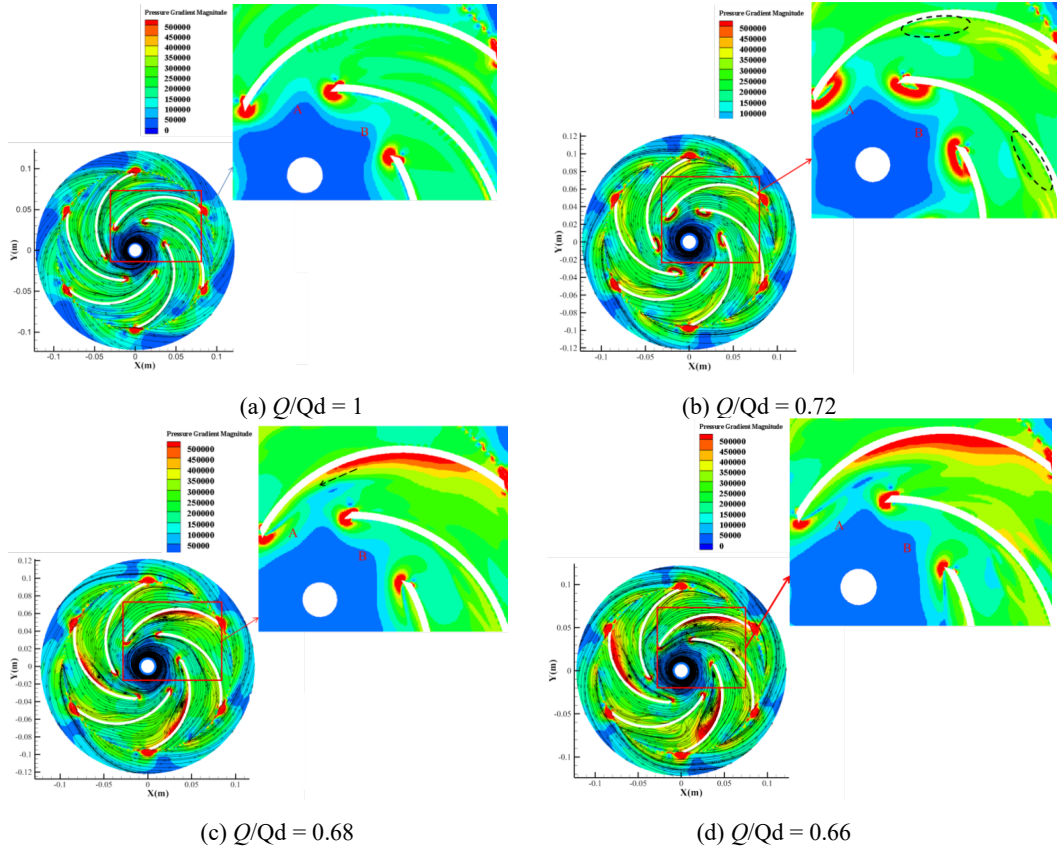


Fig. 16. Reverse pressure gradient distribution inside the impeller under the stall conditions.

## 5. CONCLUSIONS

In this study, a non-refraction rotating equipment bench with a high-frequency PIV system and SAS-SST turbulence model has been used to study the stall inception, evolution process and mechanism in a centrifugal pump impeller.

First, through the developed high-frequency PIV system and the non-refraction rotating equipment bench, the entire process of the stall (from initiation, development, and evolution to final stability) was explained by setting a tiny rate interval of  $0.005Q_d$ . After comparing the instantaneous velocity field at different times, it appears that when the flow rate remains fixed, the shape and number of the vortex in the impeller flow passage remain basically unchanged; this conforms to the typical fixed stall characteristics. As the impeller inlet rate decreases continuously, flow separation begins to occur on the suction side blade. When the flow separation on the suction side of the blade occurs, the impeller inlet does not show a vortex structure due to the increase in the attack angle. The appearance of flow separation results in a low-velocity area near the suction side blade. The low-velocity area further evolved into a vortex structure which causes the impeller passage to be blocked. The results show that when a significant stall vortex appeared near the passage suction side, the impeller inlet angle of attack still maintains a good inflow condition.

For the impeller with uniform circumferential flow, as the flow rate decreases, the flow separation phenomenon occurs and each flow passage tends to stall. However, when one of the passages emerges stall, the adjacent passage exits the stall state immediately. It appears that in the initial stage of the stall, there is a strong flow rate exchange at the passage inlet between adjacent flow passages. For the initial stage, there are two vortexes in the stall passage. One is near the leading edge of the impeller; the other is located in the middle of the suction side blade. As the rate decreases, the size of both vortexes increases. Yet, the vortex structure at the middle position of the suction blade is much larger than that at the inlet position. Finally, the two vortexes merge into a large one, which stays at the impeller inlet. Therefore, the stall vortex at the blade inlet originates from the middle position of the suction side blade, rather than being directly generated due to attack angle at the inlet. The vortex structure at the inlet of the impeller has an important impact on the distribution of other vortex structures that subsequently appear in impeller passage.

Based on experimental results, the SAS-SST hybrid model is used to simulate several rate conditions at the stall initial stage and explains the stall mechanism. The results show that as the flow rate decreases, the increasing reversed pressure gradient and the high-pressure zone move along the suction of the blade towards the impeller inlet; also, the kinetic energy of the fluid is constantly decreasing. When the fluid does not have enough kinetic energy to maintain its continuous flow along the suction surface, flow separation occurs on the suction side and there is a high-pressure zone and a higher

reversed pressure gradient at the location of flow separation. The pressure distribution is the critical cause of changing the flow state. Therefore, the combined effect of the increase of the impeller entrance attack angle and the increasing reverse pressure is the direct cause of the stall. The essence of the stall in the flow passage impeller conforms to the boundary layer separation theory.

## ACKNOWLEDGMENTS

The study was financially supported by the National Natural Science Foundation of China (Grant No. 51679240, Grant No. 51836010 and Grant No. 51809268), and Joint Fund of State Key Lab of Hydrosience and Institute of Internet of Waters Tsinghua-Ningxia Yinchuan (Grant No. sklhse-2020-low06).

## REFERENCE

- Abernethy, R. B., R. P. Benedict and R. B. Dowdell (1985). ASME Measurement Uncertainty. *ASME-Journal of Fluids* 107(2), 161–164.
- Byskov, R. K., C. B. Jacobsen and N. Pedersen (2003). Flow in a centrifugal pump impeller at design and off-design conditions-Part I: particle image velocimetry (PIV) and laser doppler velocimetry (LDV). *Measurements. ASME-Journal of Fluids Engineering* 125(1), 61-72
- Byskov, R. K., C. B. Jacobsen, and N. Pedersen (2003). Flow in a Centrifugal Pump Impeller at Design and Off-Design Conditions—Part II: Large Eddy Simulations. *Journal of Fluids Engineering* 125(1), 73-83.
- Cui, D. and D. Liang (2013). Flow in a Low Specific Speed Centrifugal Pump Using PIV. *Advances in Mechanical Engineering* (5).
- Dazin, A., G. Cavazzini., G. Pavesi., P. Dupont., S. Coudert., G. Ardizzon., G. Caignaert and G. Bois (2011). High-speed stereoscopic PIV study of rotating instabilities in a radial vaneless diffuser. *Experiments in Fluids* 51(1), 83-93.
- Emmons, H. W., C. E. Pearson and H. P. Grant (1955). Compressor surge and stall propagation. *ASME Paper-No.* 53-A-65, 1955.
- Feng, J. J., F. K. Benra and H. J. Dohmen (2010). Application of Different Turbulence Models in Unsteady Flow Simulations of a Radial Diffuser Pump. *Forschung im Ingenieurwesen.* 74(3), 123-133.
- Guo, S. J. and M. Yoshiyuki (2005). Experimental Investigations on Pressure Fluctuations and Vibration of the Impeller in a Centrifugal Pump with Vaned Diffusers. *JSME International Journal Series B Fluids and Thermal Engineering* 48(1), 136-143.
- Huang, X. B., Z. Q. Liu and W. Yang (2015). Comparative study of SGS models for simulating the flow in a centrifugal-pump

- impeller using single passage. *Engineering Computations* 32(7), 2120-2135.
- Takeshi, S., Y. Yoshiki., Y. Yoshinobu., N. Yuki and M. Tatsuhito (2002). Numerical Study of Rotating Stall in a Pump Vaned Diffuser. *Journal of Fluids Engineering* 124(2), 363-370.
- Krause, N., K. Zähringer and E. Pap (2005). Time-resolved particle imaging velocimetry for the investigation of rotating stall in a radial pump. *Experiments in Fluids* 39(2), 192-201.
- Keller, J., E. Blanco., R. Barrio and J. Parrondo (2014). PIV measurements of the unsteady flow structures in a volute centrifugal pump at a high flow rate. *Experiments in fluids* 55(10), 1820.
- Luo, H. Y., R. Tao., J. D. Yang and Z. W. Wang (2020). Influence of Blade Leading-Edge Shape on Rotating-Stalled Flow Characteristics in a Centrifugal Pump Impeller. *Applied Sciences* 10(5635), 5635.
- Lucius, A. (2010). Unsteady CFD simulations of a pump in part load conditions using scale-adaptive simulation. *International Journal of Heat and Fluid Flow* 31(6), 1113-1118.
- Menter, F. R. and Y. Egorov (2010). The Scale-Adaptive Simulation Method for Unsteady Turbulent Flow Predictions. Part 1: Theory and Model Description. Flow. *Turbulence and Combustion* 85(1), 113-138.
- Menter, F. R. and Y. Egorov (2005). A Scale Adaptive Simulation Model using Two-Equation Models, 43rd AIAA Aerospace Sciences Meeting and Exhibit.
- Mathias, O., K. Alexander, E. Wito and T. Holger (2012). IEEE Visualization Contest Winner: Visualizing Unsteady Vortical Behavior of a Centrifugal Pump. *IEEE computer graphics and applications* 32(5), 12-19.
- Maitre, T., E. Amet and C. Pellone (2013). Modeling of the flow in a darrieus water turbine: wall grid refinement analysis and comparison with experiments. *Renewable Energy* 51(2), 497-512.
- Paone, N., M. L. Riethmuller and R. A. Braembussche (1989). Experimental investigation of the flow in the vaneless diffuser of a centrifugal pump by particle image displacement velocimetry. *Experiments in Fluids* 70, 371-378.
- Sinha, M. and J. Katz (2000). Quantitative Visualization of the Flow in a Centrifugal Pump with Diffuser Vanes—I: On Flow Structures and Turbulence. *ASME-Journal of Fluids Engineering* 122, 97–107.
- Tanaka, H. (2011). Vibration behavior and dynamic stress of runners of very high head reversible pump-turbines. *International Journal of Fluid Machinery and Systems* 4(2), 289-306.
- Westra, R. W., L. Broersma., K. van Andel and N. P. Kruyt (2010). PIV measurements and CFD computations of secondary flow in a centrifugal pump impeller. *Journal of Fluids Engineering* 132(6), 061104.
- Wang, Y.P., H. Yang, B. Chen, P.L. Gao, H. Chen and Z.C. Zhu (2019). Analysis of vortices formed in flow passage of a five-bladed centrifugal water pump by means of PIV method. *AIP Advances* 9(7), 075011.
- Wang, H. and H. Tsukamoto (2003). Experimental and Numerical Study of Unsteady Flow in Diffuser Pump at off Design Conditions. *ASME Journal of Fluids Engineering* 125(5), 767-778.
- Xia, L. S., Y. G. Cheng and X. X. Zhang (2014). Numerical analysis of rotating stall instabilities of a pump- turbine in pump mode. *27th Iahr Symposium On Hydraulic Machinery And Systems (IAHR 2014)*, 1-7.
- Younsi, M., A. Djerrada., T. Belamri and F. Menter (2008). Application of the SAS turbulence model to predict the unsteady flow field behaviour in a forward centrifugal fan. *International Journal of Computational Fluid Dynamics* 22(9), 639-648.
- Zhao, X. R., Y. X. Xiao, Z. W. Wang, Y. Y Luo and L. Cao (2018). Unsteady Flow and Pressure Pulsation Characteristics Analysis of Rotating Stall in Centrifugal Pumps Under Off-Design Conditions. *Journal of Fluids Engineering* 140(2), 021105.
- Zhang, N., B. Gao, L. Zhong, N. Dan and Q.F. Jiang (2018) Unsteady flow structure and its evolution in a low specific speed centrifugal pump measured by PIV. *Experimental Thermal and Fluid Science* 97, 133-144.
- Zhou, P. J., F. J. Wang, Z. J. Yang and J. G. Mou (2017). Investigation of rotating stall for a centrifugal pump impeller using various SGS models. *Journal of Hydrodynamics, Ser. B*, 29(2), 235-242.
- Zhang, N., M. G. Yang., B. Gao., L. Zhong and N. Dan (2014). Unsteady Pressure Pulsation and Rotating Stall Characteristics in a Centrifugal Pump with Slope Volute. *Advances in Mechanical Engineering*.